Change Detection in Synthetic Aperture Radar Images based on Image Fusion and Fuzzy Clustering

Maoguo Gong, *Member, IEEE*, Zhiqiang Zhou, and Jingjing Ma

***Abstract*—This paper presents an unsupervised distribution-free change detection approach for synthetic aperture radar (SAR) images based on an image fusion strategy and a novel fuzzy clustering algorithm. The image fusion technique is introduced to generate a difference image by using complementary information from a mean-ratio image and a log-ratio image. In order to restrain the background information and enhance the information of changed regions in the fused difference image, wavelet fusion rules based on an average operator and minimum local area energy are chosen to fuse the wavelet coefficients for a low-frequency band and a high-frequency band, respectively. A reformulated fuzzy local-information C-means clustering algorithm is proposed for classifying changed and unchanged regions in the fused difference image. It incorporates the information about spatial context in a novel fuzzy way for the purpose of enhancing the changed information and of reducing the effect of speckle noise. Experiments on real SAR images show that the image fusion strategy integrates the advantages of the log-ratio operator and the mean-ratio operator and gains a better performance. The change detection results obtained by the improved fuzzy clustering algorithm exhibited lower error than its preexistences.**

***Index Terms*—Clustering, fuzzy C-means (FCM) algorithm, image change detection, image fusion, synthetic aperture radar (SAR).**

I. Introduction

IMAGE change detection is a process that analyzes images of the same scene taken at different times in order to identify changes that may have occurred between the considered acquisition dates [1]. In the last decades, it has attracted widespread interest due to a large number of applications in diverse disciplines such as remote sensing [2]–[10], medical diagnosis [11], [12], and video surveillance [13], [14]. With the development of remote sensing technology, change detection in remote sensing images becomes more and more important [2]–[10]. Among them, change detection in synthetic aperture radar (SAR) images exhibits some more difficulties than optical ones due to the fact that SAR images suffer from the presence of the speckle noise. However, SAR sensors are independent of atmospheric and sunlight conditions, which make the change detection in SAR images still attractive [4]–[8].

As mentioned in the literature, unsupervised change detection in SAR images can be divided into three steps: 1) image preprocessing; 2) producing difference image between the multitemporal images; and 3) analysis of the difference image. The tasks of the first step mainly include coregistration, geometric corrections, and noise reduction. In the second step, two coregistered images are compared pixel by pixel to generate the difference image. For the remote sensing images, differencing (subtraction operator) and rationing (ratio operator) are well-known techniques for producing a difference image. In differencing, changes are measured by subtracting the intensity values pixel by pixel between the considered couple of temporal images. In rationing, changes are obtained by applying a pixel-by-pixel ratio operator to the considered couple of temporal images. However, in the case of SAR images, the ratio operator is typically used instead of the subtraction operator since the image differencing technique is not adapted to the statistics of SAR images and nonrobust to calibration errors [15], [16]. In addition, because of the multiplicative nature of speckles, the ratio image is usually expressed in a logarithmic or a mean scale [4]–[8]. In the third step, changes are usually detected by applying a decision threshold to the histogram of the difference image. Several thresholding methods have been proposed in order to determine the threshold in an unsupervised manner, such as Otsu, the Kittler and Illingworth minimum-error thresholding algorithm (K&I), and the expectation maximization (EM) algorithm [17].

In general, it appears clearly from the literature that the whole performance of SAR-image change detection is mainly relied on the quality of the difference image and the accuracy of the classification method. In order to address the two issues, in this paper, we propose an unsupervised distribution-free SAR-image change detection approach. It is unique in the following two aspects: 1) producing difference images by fusing a mean-ratio image and a log-ratio image, and 2) improving the fuzzy local-information c-means (FLICM) clustering algorithm [18], which is insensitive to noise, to identify the change areas in the difference image, without any distribution assumption.

This paper is organized into five sections. In the next section, the main steps of the proposed approach and our motivation will be introduced. Section III will describe the proposed method in details, and in Section IV, experimental results on real multitemporal SAR images will be described to demonstrate the effectiveness of the proposed approach. The last section presents our conclusions.

Manuscript received June 22, 2011; revised September 06, 2011 and September 14, 2011; accepted September 19, 2011. Date of publication October 06, 2011; date of current version March 21, 2012. This work was supported in part by the National High Technology Research and Development Program of China under Grant 2009AA12Z210, the Program for New Century Excellent Talents in University under Grant NCET-08-0811, the Program for New Scientific and Technological Star of Shaanxi Province under Grant 2010KJXX-03, and the Fundamental Research Funds for the Central Universities under Grant K50510020001. The associate editor coordinating the review of this manuscript and approving it for publication was Dr. Ferran Marques.

The authors are with the Key Laboratory of Intelligent Perception and Image Understanding of Ministry of Education, Xidian University, Xi'an 710071, China (e-mail: gong@ieee.org).

Digital Object Identifier 10.1109/TIP.2011.2170702

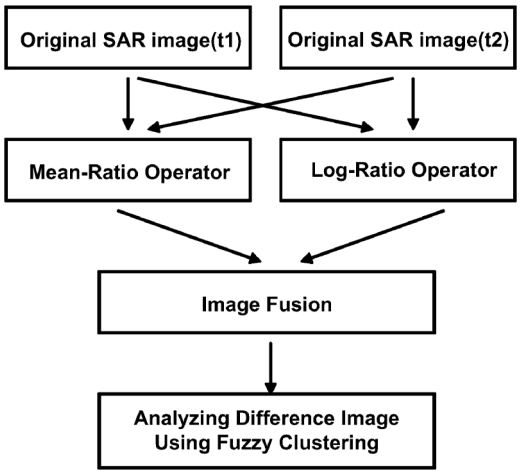

Fig. 1. Flowchart of the proposed change detection approach.

II. Motivation

Let us consider the two coregistered intensity SAR images $X_1 = \{X_1(i,j), 1 < i < H, 1 < j < W\}$ and $X_2 = \{X_2(i,j), 1 < i < H, 1 < j < W\}$ of size $H \times W$, i.e., acquired over the same geographical area at two different times t_1 and t_2, respectively. Our objective is aiming at producing a difference image that represents the change information between the two times; then, a binary classification is applied to produce a binary image corresponding to the two classes: change and unchanged. As shown in Fig. 1, the proposed unsupervised distribution-free change detection approach is made up of two main phases: 1) generate the difference image using the wavelet fusion based on the mean-ratio image and the log-ratio image; and 2) automatic analysis of the fused image by using an improved fuzzy clustering algorithm.

A. Motivation of Generating Difference Images Using Image Fusion

As mentioned in Section I, the ratio difference image is usually expressed in a logarithmic or a mean scale because of the presence of speckle noise. In the past dozen years, there was a widespread concern over the logarithm of the ratio image since the log-normal model was considered as a heuristic parametric probability distribution function for SAR intensity and amplitude distributions [19]. With the log-ratio operator, the multiplicative speckle noise can be transformed in an additive noise component. Furthermore, the range of variation of the ratio image will be compressed and thereby enhances the low-intensity pixels, and in [8], authors proposed a ratio mean detector (RMD), which is also robust to speckle noise. This detector assumes that a change in the scene will appear as a modification of the local mean value of the image. Both methods have yielded effective results for the change detection in SAR imagery but still have some disadvantages: The logarithmic scale is characterized by enhancing the low-intensity pixels while weakening the pixels in the areas of high intensity; therefore, the distribution of two classes (changed and unchanged) could be made more symmetrical. However, the information of changed regions that is obtained by the log-ratio image may not be able to reflect the real changed trends in the maximum extent because of the weakening in the areas of high-intensity pixels. As for the RMD, the background (unchanged regions) of mean-ratio image is quite rough, for the ratio technique may emphasize the differences in the low intensities of the temporal images (e.g., $150/15 = 10$ and $50/5 = 10$). In general, the underlying idea of the optimal difference image is that unchanged pixels exhibit small values, whereas changed areas exhibit larger values. That is to say that the optimal difference image should restrain the background (unchanged areas) information and should enhance the information of changed regions in the greatest extent. In order to address this problem, an image fusion technique is introduced to generate the difference image by using complementary information from the mean-ratio image and the log-ratio image in this paper. As mentioned in the literature [15], [16], the information of changed regions reflected by the mean-ratio image is relatively in accordance with the real changed trends in multitemporal SAR images. On the other hand, the information of background obtained by the log-ratio image is relatively flat on account of the logarithmic transformation. Hence, it can be concluded from the above analysis that the new difference image fused by mean-ratio image and log-ratio image could acquire better information content than the individual difference images (i.e., the mean-ratio image and the log-ratio image). The detailed description of this method will be presented in Section III-A.

B. Motivation of Analyzing Difference Image Using Fuzzy Clustering

The purpose to process the difference image is to discriminate changed regions from unchanged regions. As mentioned in Section I, the popular method to identify the changed regions, such as the K&I algorithm and the EM algorithm, is usually carried out by applying a thresholding procedure to the histogram of the difference image. It is apparent that this kind of methods requires an accurate estimation of the decision threshold. Moreover, they need to select a proper probability statistical model for distribution of change and unchanged classes in the difference image, which leads to significant restrictions on their application prospect. In this paper, a novel fuzzy c-means (FCM) clustering algorithm that is insensitive to the probability statistics model of histogram is proposed to analyze the difference image. Specifically, this method incorporates the information about spatial context to the corresponding objective function for the purpose of reducing the effect of speckle noise. Section III-B presents the further detail about this novel fuzzy clustering algorithm.

III. Methodology

In this section, we focus on describing the proposed change detection approach, which is composed of two main steps: 1) Generate the difference image based on image fusion, and 2) detect changed areas in the fused image using the improved FCM.

A. Generate the Difference Image Using Image Fusion

Image fusion refers to the techniques that obtain information of greater quality by using complementary information from

several source images so that the new fused images are more suitable for the purpose of the computed processing tasks. In the past two decades, image fusion techniques mainly take place at the pixel level of the source images [20]. In particular, multiscale transforms, such as the discrete wavelet transform (DWT), curvelets, contourlets, etc., have been used extensively for the pixel-level image fusion. The DWT isolates frequencies in both time and space, allowing detail information to be easily extracted from images. Compared with the DWT, transforms such as curvelets and contourlets are proved to have a better shift-invariance property and directional selectivity. However, their computational complexities are obviously higher than the DWT. The DWT concentrates on representing point discontinuities and preserving the time and frequency details in the image. Its simplicity and its ability to preserve image details with point discontinuities make the fusion scheme based on the DWT be suitable for the change detection task, particularly when massive volumes of source image data are to be processed rapidly.

As mentioned in the previous section, the two source images used for fusion are obtained from the mean-ratio operator and the log-ratio operator, respectively, which are commonly given by

$$X_m = 1 - \min\left(\frac{\mu_1}{\mu_2}, \frac{\mu_2}{\mu_1}\right) \tag{1}$$

$$X_l = \left|\log \frac{X_2}{X_1}\right| = |\log X_2 - \log X_1| \tag{2}$$

where μ_1 and μ_2 represent the local mean values of multitemporal SAR images X_1 and X_2, respectively.

The image fusion scheme based on the wavelet transform can be described as follows: First, we compute the DWT of each of the two source images and obtain the multiresolution decomposition of each source image. Then, we fuse corresponding coefficients of the approximate and detail subbands of the decomposed source images using the developed fusion rule in the wavelet-transform domain. In particular, the wavelet coefficients are fused using different fusion rules for a low-frequency band and a high-frequency band, respectively. Finally, the inverse DWT is applied to the fused multiresolution representation to obtain the fused result image. Fig. 2 shows the process of the proposed image fusion based on the DWT.

Here, X_m and X_l represent the mean-ratio image and the log-ratio image, respectively. H and L represent the high-pass and low-pass filters, respectively. In addition, LL represents the approximate portion of the image, and LH, HL, and HH denotes the horizontal, vertical, and diagonal direction portions, respectively. X_F denotes the fused image.

As shown in Fig. 2, each source image is decomposed into four images of the same size after one level of decomposition. The low-frequency subband X^{LL1}, which is called the approximation portion, represents the profile features of the source image. Three high-frequency subbands X^{LH1}, X^{HL1}, and X^{HH1}, which correspond to the horizontal, vertical, and diagonal direction portions, show the information about the salient features of the source image such as edges and lines. It can be inferred that the approximate coefficients of the kth decomposition level can be obtained from the approximate (low-frequency subband) and detail (high-frequency subbands)

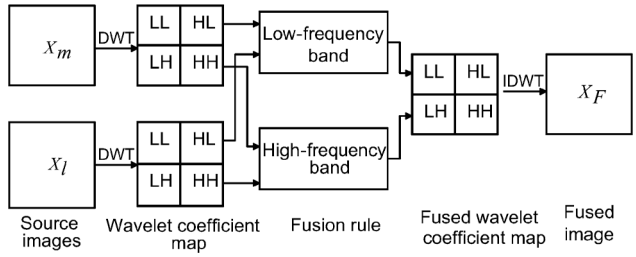

Fig. 2. Process of image fusion based on the DWT.

coefficients of the $(k+1)$th level. Furthermore, it is necessary to fuse the wavelet coefficients using different fusion rules for the low-frequency subband and the high-frequency subband, respectively, since they represent the different feature information of source images.

The key issue of the proposed approach to generate difference image is the selection of fusion rules, which should restrain the background (unchanged areas) information and should enhance the information of changed regions. In the past two decades, numerous types of fusion rules have been proposed in the literature to obtain the fused coefficient, such as the rule of selecting the maximum absolute value of corresponding wavelet coefficients and the rule of selecting the coefficients from local features such as maximum variance or contrast. The main purpose of these rules is to modify the magnitude of the coefficient of the fused image toward the maximum of that of the source images so that the gradient or edge features of the fused image are maximized. However, from the perspective of the optimal difference image, the changed and unchanged classes should be fused in different schemes, which mean that the background should be inhibited while the changed regions should be enhanced. Thus, the background information in the difference image may become rough by maximizing the gradient or edge features of the fused image in a simple way. Therefore, it is necessary to develop an adaptive scheme for the fusion of source images which could restrain the background information and enhance the information of changed regions in the greatest extent.

Here, two main fusion rules are applied: the rule of selecting the average value of corresponding coefficients for the low-frequency band, and the rule of selecting the minimum local area energy coefficient for the high-frequency band. The fusion rules can be described as follows:

$$D^F_{\mathrm{LL}} = \frac{D^m_{\mathrm{LL}} + D^l_{\mathrm{LL}}}{2} \tag{3}$$

$$D^F_{\varepsilon}(i,j) = \begin{cases} D^m_{\varepsilon}(i,j), & E^m_{\varepsilon}(i,j) < E^l_{\varepsilon}(i,j) \\ D^l_{\varepsilon}(i,j), & E^m_{\varepsilon}(i,j) \geq E^l_{\varepsilon}(i,j) \end{cases} \tag{4}$$

where m and l represent the mean-ratio image and the log-ratio image, respectively. F denotes the new fused image. D_{LL} stands for low-frequency coefficients. $D_{\varepsilon}(i,j)$ $(\varepsilon = \mathrm{LH}, \mathrm{HL}, \mathrm{HH})$ represents three high-frequency coefficients at point (i,j) in the corresponding subimages. The local area energy coefficient $E_{\varepsilon}(i,j)$ can be computed as follows:

$$E_{\varepsilon}(i,j) = \sum_{k \in N_{i,j}} [D_{\varepsilon}(k)]^2 \tag{5}$$

where $E_\varepsilon(i,j)$ represents the local area energy of the wavelet coefficient at point (i,j) in the corresponding subimage, and $N_{i,j}$ represents the local window centered on (i,j). $D_\varepsilon(k)$ denotes the value of the kth wavelet coefficient that is around the local window.

In (3) and (4), the wavelet coefficients of low frequency and high frequency are fused separately. The low-frequency subband, which represents the profile features of the source image, can significantly reflect the information of changed regions of two source difference images. Hence, in order to enhance the gradient or edge features of the changed regions, the rule of the average operator is selected to fuse the wavelet coefficients for the low-frequency subband. On the other hand, for high-frequency subbands, which indicate the information about the salient features of the source image such as edges and lines, the rule of minimum local area energy of wavelet coefficients is selected to suppress the background clutter. This rule is aimed at merging the homogeneous regions of the high-frequency portion from the mean-ratio image and the log-ratio image. Considered that the background of the log-ratio image is relatively flat (see Section II), the adoption of high frequency from the log-ratio image will help to inhibit the background in the new fused difference image to some extent.

It should be noted that the proposed approach to generate the difference image is carried out in the multiresolution decomposition. Compared with the log-ratio image, the estimation of probability statistics model for the histogram of the fused difference image may be complicated since it incorporates both the log-ratio image information and the mean-ratio image information at different resolution levels. Therefore, the thresholding technique, such as K&I and EM, may be unadapted to analyze the fused difference image for the reason that both of them assume the histogram of the difference image correspond to the certain probability statistics model. As can be seen from the above analysis, a classification method that is insensitive to the probability statistics model of histogram is needful to analyze the fused difference image. Thus, in the next section, we proposed a novel FCM clustering algorithm to analyze the difference image generated by the wavelet fusion.

B. Detect Changed Areas in the Fused Image Using the Improved FCM

The purpose to process the difference image is to discriminate changed area from unchanged area. In addition, clustering is a process for classifying objects or patterns in such a way that samples of the same cluster are more similar to one another than samples belonging to different clusters. Therefore, it can be considered that the problem of change detection can be viewed as a clustering problem where the key point is to divide the difference image data into two categories. In addition, the clustering algorithm is unrestricted by the statistical model for change and unchanged class distributions, which provides it broad prospects in SAR-image change detection. Among the clustering methods, the FCM algorithm [21] is one of the most popular methods since it can retain more information from the original image and has robust characteristics for ambiguity. However, the traditional FCM algorithm is very sensitive to noise since it does not consider any information about spatial context [18].

In recent years, many researchers have incorporated the local spatial and local gray-level information into the original FCM algorithm to compensate this drawback of FCM [18], [22], [23]. Ahmed *et al.* [22] proposed FCM_S where the objective function of the classical FCM is modified in order to compensate the intensity inhomogeneity and to allow the labeling of a pixel to be influenced by the labels in its immediate neighborhood. However, compared with the original FCM, the computational complexity of FCM_S is significantly increased since it computes the neighborhood term in each iteration step. In order to expedite the processing of FCM_S algorithm, Cai *et al.*[23] proposed the fast generalized FCM (FGFCM) algorithm, which can significantly reduce the execution time by clustering on gray-level histogram rather than on pixels; meanwhile, It is less sensitive to noise to some extent because of the introduction of local spatial information. However, from the point of view of unsupervised SAR-image change detection task, both of them have the following drawback: An artificial parameter is applied in their objective functions in order to balance between robustness to noise and effectiveness of preserving the details of the image. The selection of parameter is not easy to implement since there is no prior knowledge about the speckle noise level. Generally, the selection of the parameter has to be made by experience or by using a trial-and-error method. Recently, Krindis and Chatzis [18] have proposed a robust FLICM clustering algorithm to remedy the above shortcoming. Now, let us focus on the analysis of this algorithm and present our improvement.

1) FLICM Clustering Algorithm: The characteristic of FLICM is the use of a fuzzy local similarity measure, which is aimed at guaranteeing noise insensitiveness and image detail preservation. In particular, a novel fuzzy factor G_{ki} is introduced into the object function of FLICM to enhance the clustering performance. This fuzzy factor can be defined mathematically as follows:

$$G_{ki} = \sum_{j \in N_i} \frac{1}{d_{ij}+1}(1-u_{kj})^m \|x_j - v_k\|^2 \tag{6}$$

where the ith pixel is the center of the local window, the jth pixel represents the neighboring pixels falling into the window around the ith pixel, and d_{ij} is the spatial Euclidean distance between pixels i and j. ν_k represents the prototype of the center of cluster k, and u_{kj} represents the fuzzy membership of the gray value j with respect to the kth cluster.

It can be seen that factor G_{ki} is formulated without setting any artificial parameter that controls the tradeoff between image noise and the image details. In addition, the influence of pixels within the local window in G_{ki} is exerted flexibly by using their spatial Euclidean distance from the central pixel. Therefore, G_{ki} can reflect the damping extent of the neighbors with the spatial distances from the central pixel. However, compared with the FLICM, the artificial parameter that is applied in FCM_S and FGFCM is relatively difficult to vary adaptively with diverse spatial locations or distances from the central pixel. In general, with the application of the fuzzy factor G_{ki}, the corresponding membership values of the no-noisy pixels, as well as of the noisy pixels that is falling into the local window, will

converge to a similar value and thereby balance the membership values of the pixels that are located in the window. Thus, FLICM becomes more robust to outliers. In addition, the characteristics of FLICM include noise immunity, preserving image details without setting any artificial parameter, and being applied directly on the original image.

By using the definition of G_{ki}, the objective function of the FLICM can be defined in terms of

$$J_m = \sum_{i=1}^{N}\sum_{k=1}^{c}\left[u_{ki}^m\|x_i - v_k\|^2 + G_{ki}\right] \tag{7}$$

where ν_k represents the prototype value of the kth cluster and u_{ki} represents the fuzzy membership of the ith pixel with respect to cluster k, N is the number of the data items, and c is the number of clusters. $\|x_i - v_k\|^2$ is the Euclidean distance between object x_i and the cluster center v_k.

In addition, the calculation of the membership partition matrix and the cluster centers is performed as follows:

$$u_{ki} = \frac{1}{\sum_{j=1}^{c}\left(\frac{\|x_i-v_k\|^2+G_{ki}}{\|x_i-v_j\|^2+G_{ji}}\right)^{1/(m-1)}} \tag{8}$$

$$\nu_k = \frac{\sum_{i=1}^{N} u_{ki}^m x_i}{\sum_{i=1}^{N} u_{ki}^m} \tag{9}$$

where the initial membership partition matrix is computed randomly.

Finally, the FLICM algorithm is given as follows.

Step 1) Set the number c of the cluster prototypes, fuzzification parameter m and the stopping condition ε.
Step 2) Initialize randomly the fuzzy partition matrix.
Step 3) Set the loop counter $b = 0$.
Step 4) Compute the cluster prototypes using (9).
Step 5) Calculate the fuzzy partition matrix using (8).
Step 6) $\max\{U^{(b)} - U^{(b+1)}\} < \varepsilon$ then stop; otherwise, set $b = b + 1$, and go to step 4).

2) Modification on the FLICM: According to the analysis of the fuzzy factor G_{ki}, it can be inferred that the local gray-level information and spatial information in G_{ki} are represented by the gray-level difference and spatial distance, respectively. Furthermore, the local spatial relationship changes adaptively according to spatial distances from the central pixel. The authors of FLICM attempt to measure the damping extent of the neighbors with the spatial distances from the central pixel. For the neighborhood pixels with the same gray-level value, the greater the spatial distance is, the smaller the damping extent is, and vice versa. However, the spatial distance used to measure the damping extent of the neighbors may be unreasonable in some cases. Here, two cases are presented for examples.

Case 1) The central pixel is not noise, and some pixels within its local window may be corrupted by noise. A 3×3 window [see Fig. 3(a)] that is extracted from the noise image depicts this situation, and Fig. 3(c) depicts its damping extent of the neighbors with the spatial distances $(1/(d_{ij}+1))$. In this case, the gray values of the noisy pixels are far different from the other pixels within the window. For the noisy pixels of A and B, the gray-level difference between pixel A and the central pixel is greater than pixel B. In order to suppress the influence of the noisy pixels as far as possible, the weightings added of pixel A in G_{ki} should be able to reflect a stronger trend in contrast with the noisy pixel B. However, the damping extent of the neighbors with the spatial distances shows the opposite trend [see Fig. 3(c)].

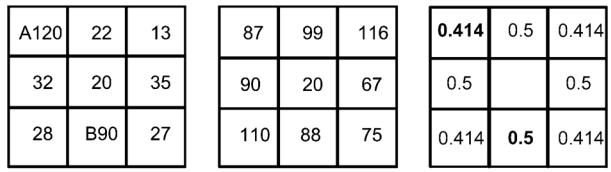

(a) (b) (c)

Fig. 3. 3×3 window with noise and their damping extent of the neighboring pixels. (a) Central pixel is not noise. (b) Central pixel is corrupted by noise. (c) Damping extent of the neighboring pixels.

Case 2) The central pixel is corrupted by noise, whereas the other pixels within its local window are homogenous and not corrupted by noise. An example that illustrates this situation is demonstrated in Fig. 3(b). In this case, the gray-level differences between the neighboring pixels and the central pixel are somewhat different. To estimate the fuzzy factor G_{ki} rigorously, the damping extent of the neighboring pixels is supposed to be treated separately. However, the damping extent of the neighbors that is reflected by the spatial distances is simply divided into two categories (0.414 and 0.5). It fails to analyze exhaustively the impact of each neighboring pixel onto the fuzzy factor G_{ki}.

The foregoing analysis highlights the importance of the accurate estimation of the fuzzy factor G_{ki} to suppress effectively the influence of the noisy pixels. In order to overcome the shortcoming mentioned above, in this paper, the local coefficient of variation is adopted to replace the spatial distance. In addition, the local coefficient of variation C_u is defined by

$$C_u = \frac{\mathrm{var}(x)}{(\bar{x})^2} \tag{10}$$

where $\mathrm{var}(x)$ and $\bar{x}$ are the intensity variance and the mean in a local window of the image, respectively.

The value of C_u reflects the gray-value homogeneity degree of the local window. It exhibits high values at edges or in the area corrupted by noise and produces low values in homogeneous regions. The damping extent of the neighbors with local coefficient of variation is measured by the areal type of the neighbor pixels located. If the neighbor pixel and the central pixel are located in the same region, such as the homogeneous region or the area corrupted by noise, the results of the local coefficient of variation obtained by them will be very close and vice versa. In general, compared with the spatial distance, the discrepancy of the local coefficient of variation between neighboring pixels and the central pixel is relatively accordance with the gray-level difference between them. In addition, it helps to

exploit more local context information since the local coefficient of variation of each pixel is computed in a local window. Here, the modified fuzzy factor G'_{ki} can be defined as

$$G'_{ki} = \begin{cases} \sum_{j\in N_i} \frac{1}{2+\min\left((C_u^j/C_u)^2,(C_u/C_u^j)^2\right)} \\ \quad \times(1-u_{kj})^m\|x_j-v_k\|^2, & \text{if } C_u^j \geq \overline{C_u} \\ \sum_{j\in N_i} \frac{1}{2-\min\left((C_u^j/C_u)^2,(C_u/C_u^j)^2\right)} \\ \quad \times(1-u_{kj})^m\|x_j-v_k\|^2, & \text{if } C_u^j < \overline{C_u} \end{cases} \tag{11}$$

where C_u is the local coefficient of variation of the central pixel, C_u^j represents the local coefficient of variation of neighboring pixels, and $\overline{C_u}$ is the mean value of C_u^j that is located in a local window. As shown in (11), the reformulated factor G'_{ki} balances the membership value of the central pixel taking into account the local coefficient of variation, as well as the gray level of the neighboring pixels. If there is a distinct difference between the results of the local coefficient of variation that are obtained by the neighboring pixel and the central pixel, the weightings added of the neighboring pixel in G'_{ki} will be increased to suppress the influence of outlier; thereby, the reformulated FLICM, i.e., termed as RFLICM, is expected to be more robust to its preexistence.

Finally, by taking the place of G_{ki} in FLICM with the new fuzzy factor G'_{ki}, the RFLICM algorithm can be summarized as follows.

Step 1) Set values for c, m, and ε.
Step 2) Initialize randomly the fuzzy partition matrix and set the loop counter $b = 0$.
Step 3) Calculate the cluster prototypes using (9).
Step 4) Compute the partition matrix using (8).
Step 5) $\max\{U^{(b)} - U^{(b+1)}\} < \varepsilon$ then stop; otherwise, set $b = b + 1$, and go to step 3).

IV. Experimental Study

In this section, in order to validate the effectiveness of the proposed SAR-image change detection method, we will show the performance of the proposed methods by presenting numerical results on three data sets.

The first data set represents a section (301 × 301 pixels) of two SAR images acquired by the European Remote Sensing 2 satellite SAR sensor over an area near the city of Bern, Switzerland, in April and May 1999, respectively. Between the two dates, the River Aare flooded entirely parts of the cities of Thun and Bern and the airport of Bern. Therefore, the Aare Valley between Bern and Thun was selected as a test site for detecting flooded areas. The available ground truth (reference image), which was shown in Fig. 4(c), was created by integrating prior information with photo interpretation based on the input images Fig. 4(a) and (b).

The second data set is a section (290 × 350 pixels) of two SAR images over the city of Ottawa acquired by the Radarsat SAR sensor. They were provided by the Defence Research and Development Canada in Ottawa, Canada. These images were registered by the automatic registration algorithm from A.U.G. Signals Ltd. that is available through the distributed computing at www.signalfusion.com. There are roughly two regions in these images, i.e., water and land. The available ground truth (reference image), i.e., shown in Fig. 5(c), was created by integrating prior information with photograph interpretation based on the input images Fig. 5(a) and (b).

The third data set used in the experiments consisted of two SAR images acquired by Radarsat-2 at the region of Yellow River Estuary in China in June 2008 and June 2009, respectively. The original size of these two SAR images acquired by Radarsat-2 is 7666 × 7692. They are too huge to show the detail information in such small pages. We select one repressive area of size 257 × 289 pixels [see Fig. 6(a) and (b)] to compare the change detection results obtained by different approaches. The available ground truth (reference image), i.e., shown in Fig. 6(c), was created by integrating prior information with photo interpretation based on the input images Fig. 6(a) and (b). It should be noted that the two images considered are single-look image and four-look image, respectively. This means that the influence of speckle noise on the image acquired in 2009 is much greater than the one acquired in 2008. The huge difference of speckle noise level between the two images used may complicated the processing of change detection.

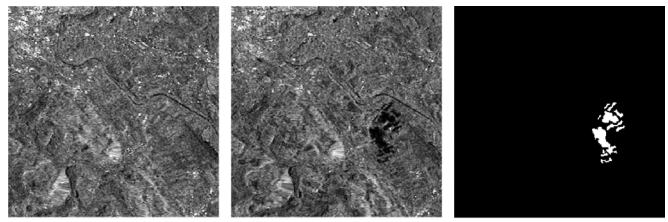

(a) (b) (c)

Fig. 4. Multitemporal images relating to the city of Bern used in the experiments. (a) Image acquired in April 1999 before the flooding. (b) Image acquired in May 1999 after the flooding. (c) Ground truth.

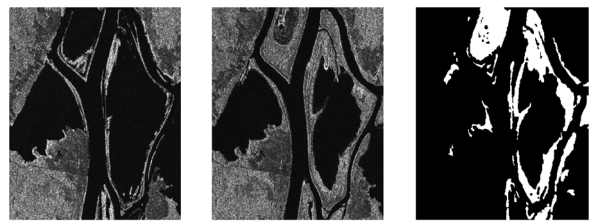

(a) (b) (c)

Fig. 5. Multitemporal images relating to Ottawa used in the experiments. (a) Image acquired in July 1997 during the summer flooding. (b) Image acquired in August 1997 after the summer flooding. (c) Ground truth.

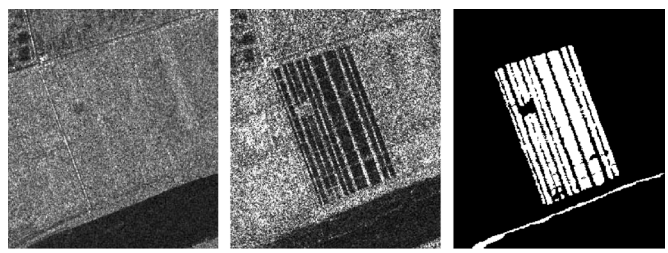

(a) (b) (c)

Fig. 6. Multitemporal images relating to the Yellow River Estuary used in the experiments. (a) Image acquired in June 2008. (b) Image acquired in June 2009. (c) Ground truth.

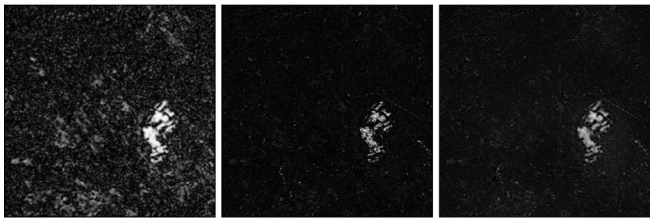

(a) (b) (c)

Fig. 7. Difference images of the Bern data set generated from (a) mean-ratio operator, (b) log-ratio operator, and (c) wavelet fusion.

Two experiments have been carried out, i.e., aimed at different purposes. The first experiment is aimed at the analysis of the effectiveness of the wavelet fusion strategy to generate the difference image. In addition, we compared the change detection performance of our algorithm with other two methods, including the mean-ratio operator and the log-ratio operator. A 3 $\times$ 3 sliding window is selected to compute the local area energy of the wavelet coefficient. In particular, two simple classification methods, i.e., K-means and Otsu, are applied to evaluate the change detection results that are obtained by the difference images mentioned above. In the second experiment, we analyzed the impact of the RFLICM algorithm onto the change detection results of the fused difference image. To verify the suitability of the proposed approach for the fused difference image, we presented comparative analysis of the performances of our proposed algorithm with that of the traditional FCM algorithm and the FLICM algorithm.

The quantitative analysis of change detection results is set as follow. These criteria are from [24]. First, we calculate the false negatives (FN, changed pixels that undetected). Second, we calculate the false positives (FP, unchanged pixels wrongly classi?ed as changed). Third, we calculate the percentage correct classification (PCC). It is given by

$$\mathrm{PCC} = (\mathrm{TP} + \mathrm{TN}) / (\mathrm{TP} + \mathrm{FP} + \mathrm{TN} + \mathrm{FN}). \qquad (12)$$

Here, TP is short for true positives, which is the number of pixels that are detected as the changed area in both the reference image and the result. TN is short for true negatives, which is the number of pixels that are detected as the unchanged area in both the reference image and the result.

For accuracy assessment, kappa statistic, which is a measure of accuracy or agreement based on the difference between the error matrix and chance agreement [25], is reported to take into account of commission and omission errors. If the change detection map and the reference image are in complete agreement, then the kappa value is 1. If there is no agreement among the change detection map and the reference image, the kappa value is 0.

A. Results on the bern data set

In the first experiment, we analyzed the effectiveness of wavelet image fusion technique to generate the difference image. The difference images generated by the three different methods (mean-ratio, log-ratio, wavelet fusion) have been shown in Fig. 7. The gut feeling of the fused difference image [see Fig. 7(c)] is infusive. The step changes [6] corresponding to a strong modification of the land cover that occurred between two images is well reflected, and then the background (unchanged regions) in fused image is inhibited to a certain degree with the use of wavelet coefficients of log-ratio image. As shown in Tables I and II, the change detection results of the fused difference image were compared with the ones generate from mean-ratio operator and log-ratio operator by Otsu and K-means, respectively. It can be seen from the analysis of the PCC that, the change detection results of mean-ratio difference image that achieved by both methods was disastrous. For the log-ratio operator, the PCC yielded was equal to 99.27% for Otsu, and 99.24% for K-means. And the proposed approach resulted in the highest PCC (99.35% for Otsu and 99.36% for K-means) and kappa (0.781 for Otsu and 0.784 for K-means). By a visual analysis of Figs. 8 and 9, we can have a better understanding of the behavior of the three different methods.

TABLE I
CHANGE DETECTION RESULTS OF THE BERN DATA SET OBTAINED BY OTSU BASED ON THE THREE DIFFERENCE IMAGES

Difference Image	FP	FN	PCC	Kappa
Mean-Ratio	14782	8	83.68%	0.125
Log-Ratio	361	326	99.24%	0.703
Wavelet Fusion	514	78	99.35%	0.781

TABLE II
CHANGE DETECTION RESULTS OF THE BERN DATA SET OBTAINED BY K-MEANS BASED ON THE THREE DIFFERENCE IMAGES

Difference Image	FP	FN	PCC	Kappa
Mean-Ratio	15552	8	82.83%	0.107
Log-Ratio	363	329	99.24%	0.703
Wavelet Fusion	503	77	99.36%	0.784

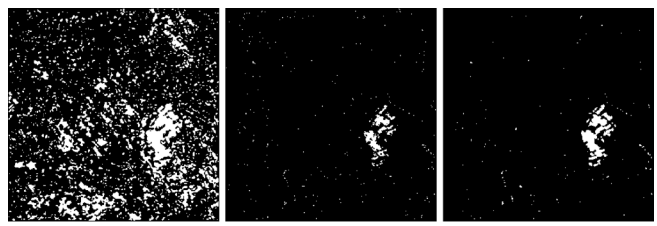

(a) (b) (c)

Fig. 8. Change detection results of the Bern data set based on the three difference images obtained by Otsu. (a) Based on the mean-ratio operator. (b) Based on the log-ratio operator. (c) Based on wavelet fusion.

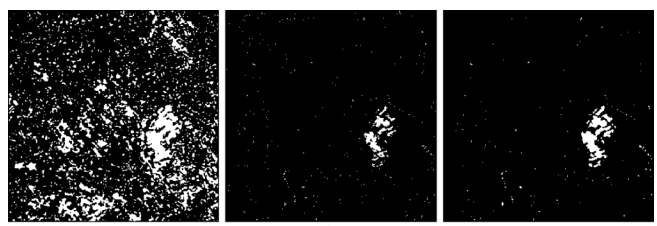

(a) (b) (c)

Fig. 9. Change detection results of the Bern data set based on the three difference images obtained by K-means. (a) Based on the mean-ratio operator. (b) Based on the log-ratio operator. (c) Based on wavelet fusion.

(a) (b) (c)

Fig. 10. Change detection results of the Bern data set achieved by (a) FCM, (b) FLICM, and (c) proposed RFLICM.

TABLE III
COMPARISON OF THE CHANGE DETECTION RESULTS ON THE BERN DATA SET ACQUIRED BY THE FCM, FLICM, AND RFLICM

Method	FP	FN	PCC	Kappa
FCM	507	61	99.37%	0.790
FLICM	137	169	99.66%	0.867
RFLICM	133	159	99.68%	0.871

Figs. 8(a) and 9(a) depict the change detection results obtained from the mean-ratio image, which reveal that it has more spots than the other two methods because of the effect of the speckle phenomenon. As can be seen from Figs. 8(b) and 9(b), the change detection maps obtained from the log-ratio image have lesser spots because of the logarithmic transformation. However, it also caused the loss of information in changed areas since the operation of log-ratio may abate the high-intensity pixels. The change detection maps yield from the wavelet fusion image are shown in Figs. 8(c) and 9(c). As can be concluded from above analysis, the method that we proposed can effectively reduce the errors in the change detection results.

To assess the impact of RFLICM algorithm on the results of SAR-image change detection which based on the wavelet fusion difference image, in the second experiment, a comparison was carried out among traditional FCM, FLICM and RFLICM. According to Fig. 10(a), the change detection map achieved by traditional FCM contains lots of spots. This is explained by the fact that it fail to consider any information about spatial context. By contrast, by incorporating the local information, the change detection maps generated by FLICM [Fig. 10(b)] and RFLICM [Fig. 10(c)] were robust to the outliers. As shown in Table III, it depicts the behavior of kappa, PCC, FP and FN among these three methods. The PCC yielded by RFLICM, FLICM and FCM were equal to 99.68%, 99.66% and 99.37%, respectively. RFLICM outperforms FLICM and FCM obviously.

B. Results on the Ottawa Data Set

The first experiment is aimed at analyzing the effectiveness of the proposed approach that is based on the wavelet fusion. Fig. 11 represents the difference images generated by the mean ratio, the log ratio, and the wavelet fusion. The change detection results generated from the three difference images have been shown in Figs. 12 and 13. In particular, as shown in Figs. 12(a) and 13(a), due to the reason of image speckle noise, the change detection maps generated from the mean-ratio difference image swarmed with isolated spots, whether using Otsu or K-means. As for the log-ratio difference image, the change detection maps

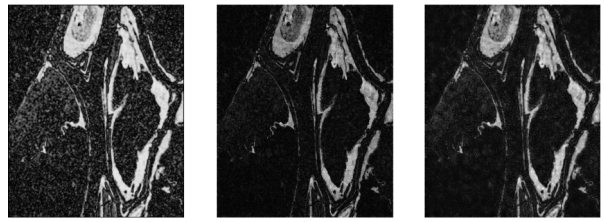

(a) (b) (c)

Fig. 11. Difference images of the Ottawa data set generated from (a) mean-ratio operator, (b) log-ratio operator, and (c) wavelet fusion.

(a) (b) (c)

Fig. 12. Change detection results of the Ottawa data set based on the three difference images obtained by Otsu. (a) Based on the mean-ratio operator. (b) Based on the log-ratio operator. (c) Based on wavelet fusion.

(a) (b) (c)

Fig. 13. Change detection results of the Ottawa data set based on the three difference images obtained by K-means. (a) Based on the mean-ratio operator. (b) Based on the log-ratio operator. (c) Based on wavelet fusion.

TABLE IV
CHANGE DETECTION RESULTS OF THE OTTAWA DATA SET OBTAINED BY OTSU BASED ON THE THREE DIFFERENCE IMAGES

Difference Image	FP	FN	PCC	Kappa
Mean-Ratio	2426	256	97.36%	0.905
Log-Ratio	909	1942	97.19%	0.890
Wavelet Fusion	840	1132	98.06%	0.925

TABLE V
CHANGE DETECTION RESULTS OF THE OTTAWA DATA SET OBTAINED BY K-MEANS BASED ON THE THREE DIFFERENCE IMAGES

Difference Image	FP	FN	PCC	Kappa
Mean-Ratio	2525	242	97.27%	0.902
Log-Ratio	912	1926	97.20%	0.890
Wavelet Fusion	896	1073	98.06%	0.926

are illustrated in Figs. 12(b) and 13(b). The problem of losing information in change regions persists, with the fact that the missed alarms caused by Otsu and K-means were up to 1942 pixels and 1926 pixels, respectively. Conversely, the change

(a) (b) (c)

Fig. 14. Change detection results of Ottawa data set achieved by (a) FCM, (b) FLICM, and (c) proposed RFLICM.

TABLE VI
COMPARISON OF THE CHANGE DETECTION RESULTS ON THE OTTAWA DATA SET OBTAINED BY THE FCM, FLICM, AND RFLICM

Method	FP	FN	PCC	Kappa
FCM	781	1084	98.16%	0.929
FLICM	270	994	98.75%	0.949
RFLICM	207	761	99.05%	0.962

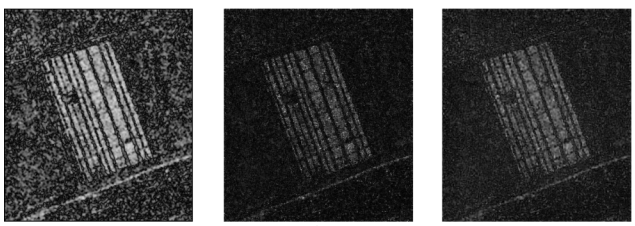

(a) (b) (c)

Fig. 15. Difference images of the Yellow River Estuary data set generated from (a) mean-ratio operator, (b) log-ratio operator, and (c) wavelet fusion.

detection maps achieved from wavelet fusion [see Figs. 12(c) and 13(c)] are very close to the ground-truth map illustrated in Fig. 5(c). As reported in Tables IV and V, the maximum PCC and kappa are achieved by the fused difference image.

In the second experiment, to assess the suitability of the presented RFLICM algorithm for the wavelet fusion difference image, a comparison analysis was carried out on two other methods (FCM and FLICM). Change detection maps obtained by FCM, which is sensitive to noise [illustrated in Fig. 14(a)], confirm the necessity of incorporating the information about spatial context. As reported in Table VI, the proposed RFLICM resulted in the highest PCC and kappa. The quantitative analysis confirms the suitability of the RFLICM algorithm on the fused difference image.

C. Results on the Yellow River Estuary Data Set

Unlike the Bern or Ottawa data sets, the influence of speckle noise on the image acquired in 2009 is much greater than the one acquired in 2008 since the two images considered are a single-look image and a four-look image, respectively. It represents a more complicated situation to assess the effectiveness of the proposed approach. Fig. 15 represents the difference images generated by the mean ratio, the log ratio, and the wavelet fusion. The change detection maps achieved by FLICM and RFLICM are illustrated in Figs. 16 and 17, respectively.

(a) (b) (c)

Fig. 16. Change detection results of the Yellow River Estuary data set based on the three difference images obtained by FLICM. (a) Based on the mean-ratio operator. (b) Based on the log-ratio operator. (c) Based on wavelet fusion.

(a) (b) (c)

Fig. 17. Change detection results of the Yellow River Estuary data set based on the three difference images obtained by RFLICM. (a) Based on the mean-ratio operator. (b) Based on the log-ratio operator. (c) Based on wavelet fusion.

TABLE VII
CHANGE DETECTION RESULTS OF THE YELLOW RIVER ESTUARY DATA SET OBTAINED BY FLICM BASED ON THE THREE DIFFERENCE IMAGES

Difference Image	FP	FN	PCC	Kappa
Mean-Ratio	3822	2570	91.39%	0.717
Log-Ratio	328	3820	94.42%	0.788
Wavelet Fusion	324	2750	95.86%	0.850

TABLE VIII
CHANGE DETECTION RESULTS OF THE YELLOW RIVER ESTUARY DATA SET OBTAINED BY RFLICM BASED ON THE THREE DIFFERENCE IMAGES

Difference Image	FP	FN	PCC	Kappa
Mean-Ratio	2688	3284	91.96%	0.721
Log-Ratio	327	3602	94.71%	0.802
Wavelet Fusion	316	2545	96.15%	0.860

As shown in Figs. 16 and 17, lots of spots are contained in the changed detection map that is generated from the mean-ratio operator [see Figs. 16(a) and 17(a)]. On the other hand, for the change detection maps generated from the log ratio [see Figs. 16(b) and 17(b)], too much information has been lost, although it exhibits less spots. By comparison, the difference image generated by wavelet fusion can reflect the real change trend as well as mitigate the impact of speckle noise [see Figs. 16(c) and 17(c)]. Moreover, as reported in Tables VII and VIII, the fused difference image resulted in the highest PCC and kappa.

The visual and quantitative results on the Yellow River estuary data set confirm the suitability of the RFLICM algorithm on the fused difference image. As a matter of fact, RFLICM and FLICM incorporate both local spatial and gray information to find a tradeoff between detail preservation and noise removal. The proposed RFLICM attends to evaluate the local information more precisely than FLICM.

V. Concluding Remarks

In this paper, we have presented a novel SAR-image change detection approach based on image fusion and an improved fuzzy clustering algorithm, which is quite different from the existing methods. First, for the wavelet fusion approach that we proposed, the key idea is to restrain the background (unchanged areas) information and to enhance the information of changed regions in the greatest extent. As mentioned in the literature, the information of changed regions reflected by the mean-ratio image is relative in accordance with the real changed trends in multitemporal SAR images. On the other hand, the information of background obtained by the log-ratio image is relatively flat on account of the logarithmic transformation. Hence, complementary information from the mean-ratio image and the log-ratio image is utilized to fuse a new difference image. Compared with other existing methods (mean ratio and log ratio), the proposed approach can reflect the real change trend as well as restrain the background (unchanged areas). Second, in contrast with the log-ratio image and the mean-ratio image, the estimation of the probability statistics model for the histogram of the fused difference image may be complicated since it incorporates both the log-ratio and mean-ratio image information at different resolution levels. Hence, the thresholding technique, such as K&I and EM, may be unadapted to analyze the fused difference image since both of them assume the histogram of the difference image corresponding to the certain probability statistics model. Here, the RFLICM algorithm that incorporates both local spatial and gray information is proposed, which is relatively insensitive to probability statistics model. The RFLICM algorithm introduces the reformulated factor G_{ki} as a local similarity measure to make a tradeoff between image detail and noise. Compared with the original algorithms, RFLICM is able to incorporate the local information more exactly.

The experiment results show that the proposed wavelet fusion strategy can integrate the advantages of the log-ratio operator and the mean-ratio operator and gain a better performance. The change detection results obtained by the RFLICM exhibited less spots than its preexistence (i.e., FLICM) since it is able to incorporate the local information more exactly.

Acknowledgment

The authors would like to thank Dr. Krinidis for providing their FLICM source codes for comparisons and the editors and anonymous reviewers for their valuable comments and helpful suggestions, which greatly improved the quality of this paper.

References

[1] R. J. Radke, S. Andra, O. Al-Kofahi, and B. Roysam, "Image change detection algorithms: A systematic survey," *IEEE Trans. Image Process.*, vol. 14, no. 3, pp. 294–307, Mar. 2005.

[2] L. Bruzzone and D. F. Prieto, "An adaptive semiparametric and context-based approach to unsupervised change detection in multi-temporal remote-sensing images," *IEEE Trans. Image Process.*, vol. 11, no. 4, pp. 452–466, Apr. 2002.

[3] A. A. Nielsen, "The regularized iteratively reweighted MAD method for change detection in multi- and hyperspectral data," *IEEE Trans. Image Process.*, vol. 16, no. 2, pp. 463–478, Feb. 2007.

[4] Y. Bazi, L. Bruzzone, and F. Melgani, "An unsupervised approach based on the generalized Gaussian model to automatic change detection in multitemporal SAR images," *IEEE Trans. Geosci. Remote Sens.*, vol. 43, no. 4, pp. 874–887, Apr. 2005.

[5] F. Bovolo and L. Bruzzone, "A detail-preserving scale-driven approach to change detection in multitemporal SAR images," *IEEE Trans. Geosci. Remote Sens.*, vol. 43, no. 12, pp. 2963–2972, Dec. 2005.

[6] F. Bujor, E. Trouvé, L. Valet, J. M. Nicolas, and J. P. Rudant, "Application of log-cumulants to the detection of spatiotemporal discontinuities in multitemporal SAR images," *IEEE Trans. Geosci. Remote Sens.*, vol. 42, no. 10, pp. 2073–2084, Oct. 2004.

[7] F. Chatelain, J.-Y. Tourneret, and J. Inglada, "Change detection in multisensor SAR images using bivariate Gamma distributions," *IEEE Trans. Image Process.*, vol. 17, no. 3, pp. 249–258, Mar. 2008.

[8] J. Inglada and G. Mercier, "A new statistical similarity measure for change detection in multitemporal SAR images and its extension to multiscale change analysis," *IEEE Trans. Geosci. Remote Sens.*, vol. 45, no. 5, pp. 1432–1445, May 2007.

[9] S. Marchesi, F. Bovolo, and L. Bruzzone, "A context-sensitive technique robust to registration noise for change detection in VHR multispectral images," *IEEE Trans. Image Process.*, vol. 19, no. 7, pp. 1877–1889, Jul. 2010.

[10] A. Robin, L. Moisan, and S. Le Hegarat-Mascle, "An a-contrario approach for subpixel change detection in satellite imagery," *IEEE Trans. Pattern Anal. Mach. Intell.*, vol. 32, no. 11, pp. 1977–1993, Nov. 2010.

[11] M. Bosc, F. Heitz, J. P. Armspach, I. Namer, D. Gounot, and L. Rumbach, "Automatic change detection in multimodal serial MRI: Application to multiple sclerosis lesion evolution," *Neuroimage*, vol. 20, no. 2, pp. 643–656, Oct. 2003.

[12] D. Rey, G. Subsol, H. Delingette, and N. Ayache, "Automatic detection and segmentation of evolving processes in 3-D medical images: Application to multiple sclerosis," *Med. Image Anal.*, vol. 6, no. 2, pp. 163–179, Jun. 2002.

[13] D. M. Tsai and S. C. Lai, "Independent component analysis-based background subtraction for indoor surveillance," *IEEE Trans. Image Process.*, vol. 18, no. 1, pp. 158–167, Jan. 2009.

[14] S. S. Ho and H. Wechsler, "A martingale framework for detecting changes in data streams by testing exchangeability," *IEEE Trans. Pattern Anal. Mach. Intell.*, vol. 32, no. 12, pp. 2113–2127, Dec. 2010.

[15] A. Singh, "Digital change detection techniques using remotely sensed data," *Int. J. Remote Sens.*, vol. 10, no. 6, pp. 989–1003, 1989.

[16] E. J. M. Rignot and J. J. Van Zyl, "Change detection techniques for ERS-1 SAR data," *IEEE Trans. Geosci. Remote Sens.*, vol. 31, no. 4, pp. 896–906, Jul. 1993.

[17] M. Sezgin and B. Sankur, "A survey over image thresholding techniques and quantitative performance evaluation," *J. Electron. Imag.*, vol. 13, no. 1, pp. 146–165, Jan. 2004.

[18] S. Krinidis and V. Chatzis, "A robust fuzzy local information C-means clustering algorithm," *IEEE Trans. Image Process.*, vol. 19, no. 5, pp. 1328–1337, May 2010.

[19] E. E. Kuruoglu and J. Zerubia, "Modeling SAR images with a generalization of the Rayleigh distribution," *IEEE Trans. Image Process.*, vol. 13, no. 4, pp. 527–533, Apr. 2004.

[20] G. Piella, "A general framework for multiresolution image fusion: From pixels to regions," *Inf. Fusion*, vol. 4, no. 4, pp. 259–280, Dec. 2003.

[21] J. C. Bezdek, *Pattern Recognition With Fuzzy Objective Function*. New York: Plenum, 1981.

[22] M. Ahmed, S. Yamany, N. Mohamed, A. Farag, and T. Moriarty, "A modified fuzzy C-means algorithm for bias field estimation and segmentation of MRI data," *IEEE Trans. Med. Imag.*, vol. 21, no. 3, pp. 193–199, Mar. 2002.
[23] W. Cai, S. Chen, and D. Zhang, "Fast and robust fuzzy C-means clustering algorithms incorporating local information for image segmentation," *Pattern Recognit.*, vol. 40, no. 3, pp. 825–838, Mar. 2007.
[24] P. L. Rosin and E. Ioannidis, "Evaluation of global image thresholding for change detection," *Pattern Recognit. Lett.*, vol. 24, no. 14, pp. 2345–2356, Oct. 2003.
[25] G. H. Rosenfield and A. Fitzpatrick-Lins, "A coefficient of agreement as a measure of thematic classification accuracy," *Photogramm. Eng. Remote Sens.*, vol. 52, no. 2, pp. 223–227, 1986.

Maoguo Gong (M'07) received the B.Eng. degree in electronic engineering (with first class honors) and Ph.D. degree in electronic science and technology from Xidian University, Xi'an, China, in 2003 and 2009, respectively.

Since 2006, he has been a Teacher with Xidian University. In 2008 and 2010, he was promoted as an Associate Professor and as a Full Professor, respectively, both with exceptive admission. He is currently a Full Professor with the Key Laboratory of Intelligent Perception and Image Understanding of the Ministry of Education, Xidian University. His research interests include computational intelligence with applications. His current research interests include change detection in remote sensing and medical images.

Dr. Gong is a member of the IEEE Computational Intelligence Society, an Executive Committee Member of the Natural Computation Society of Chinese Association for Artificial Intelligence, and a Senior Member of the Chinese Computer Federation. He was the recipient of the New Century Excellent Talent in University of the Ministry of Education of China, the Eighth Young Scientist Award of Shaanxi, the New Scientific and Technological Star of Shaanxi Province, the Excellent Yong Contributor of Shaanxi Province, the Elsevier Scopus Young Scientist Award in Sustainable Development of China, and the Science and Technology Award of Shaanxi Province (First Level, 2008 and 2010), etc.

Zhiqiang Zhou received the B.S. degree in electronic engineering from Xidian University, Xi'an, China, in 2009, where he is currently working toward the M.S. degree.

His research interests include change detection in remote sensing images.

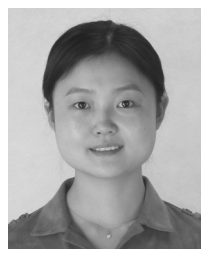

Jingjing Ma received the B.S. degree in electronic engineering from Xidian University, Xi'an, China, in 2004, where he is currently working toward the Ph.D. degree.

Her current research interests include computational intelligence and image understanding.